Letter

Difference in the in-plane anomalous Hall response in thin films of the Zintl compound EuA_2Sb_2 (A = Zn, Cd)

Hsiang Lee,[1] Shinichi Nishihaya,[1] Markus Kriener,[2] Jun Fujioka,[3] Ayano Nakamura,[1] Yuto Watanabe,[1] Hiroaki Ishizuka,[1] and Masaki Uchida[1,4,*]

[1]*Department of Physics, Institute of Science Tokyo, Tokyo 152-8551, Japan*
[2]*RIKEN Center for Emergent Matter Science (CEMS), Wako 351-0198, Japan*
[3]*Department of Materials Science, University of Tsukuba, Tsukuba 305-8577, Japan*
[4]*Toyota Physical and Chemical Research Institute, Nagakute 480-1192, Japan*

(Received 21 November 2024; revised 3 March 2025; accepted 27 May 2025; published 6 June 2025)

A recent observation of the in-plane anomalous Hall effect in the magnetic Weyl semimetal $EuCd_2Sb_2$ has drawn attention to out-of-plane orbital magnetization induced by an in-plane field component. Here, we study $EuZn_2Sb_2$, a sister compound of $EuCd_2Sb_2$, to demonstrate sensitive changes of the in-plane anomalous Hall effect on the band modulation. The Hall resistivity measured with rotating the magnetic field within the (001) principal plane of $EuZn_2Sb_2$ films exhibits a clear threefold component corresponding to the in-plane anomalous Hall effect, which is distinct from the twofold component of the planar Hall effect. The in-plane anomalous Hall effect of $EuZn_2Sb_2$ is highly contrasting to $EuCd_2Sb_2$, especially in terms of its opposite sign and field dependence, which can be explained by model calculations with different band inversion parameters. Our results pave the way for systematically controlling the in-plane anomalous Hall effect and orbital magnetization through elaborate band engineering.

DOI: 10.1103/PhysRevB.111.L241106

The Berry curvature is a local quantum geometric property of electron wave functions in the band structure, underlying many physical phenomena. Among them, the anomalous Hall effect (AHE) is one of the most representative examples of macroscopic response due to the Berry curvature in time-reversal symmetry broken systems [1–3]. For most observed AHE, the Hall vector is parallel to the direction of the magnetic field. On the other hand, the in-plane anomalous Hall effect (IAHE), with an out-of-plane Hall vector component induced by an in-plane magnetic field, is also allowed under certain symmetry conditions [4–22]. Following reports in $ZrTe_5$ [14] and VS_2/VS [15], IAHE has been recently observed in several magnetic materials, including Fe_3Sn_2 [16], $EuCd_2Sb_2$ [4], and Fe [5], uncovering a new aspect of magnetotransport. On the other hand, different mechanisms of IAHE have been suggested for each material, including an anomalous orbital polarizability model [18], an orbital magnetization model [4], and an octupole model [5].

To observe IAHE arising only from the orbital magnetization, Eu-based Zintl compounds EuA_2X_2 (A = Zn, Cd, X = P, As, Sb) with a trigonal D_{3d} lattice can be seen as a highly symmetric system suitable for studying IAHE on the principal plane, as some of the EuA_2X_2 compounds are seen as Weyl semimetals or Weyl semimetal candidates with broken time-reversal symmetry in the forced ferromagnetic state [23–27]. In the magnetic Weyl semimetal $EuCd_2Sb_2$, the observation of IAHE has been explained by field-induced out-of-plane Weyl point splitting and orbital magnetization [4]. While $EuCd_2Sb_2$ has been predicted to own four to five pairs of Weyl points [24,25], in $EuZn_2Sb_2$ the whole Cd atoms are replaced with Zn, which effectively weakens the spin-orbit coupling (SOC). Previous studies have suggested that $EuZn_2Sb_2$ hosts a pair of Weyl points above the Fermi level [27]. Also, $EuZn_2Sb_2$ shows the same in-plane A-type antiferromagnetic ordering as in $EuCd_2Sb_2$ [28–30].

Here, we report systematic transport measurements on single-domain $EuZn_2Sb_2$ thin films grown by molecular beam epitaxy (MBE). Similar to $EuCd_2Sb_2$ [25,26], $EuZn_2Sb_2$ exhibits a large out-of-plane AHE, and its Hall angle increases upon a decrease in hole density. On the other hand, a threefold IAHE response with respect to the in-plane field rotation emerges with an opposite sign and different field dependence in stark contrast to $EuCd_2Sb_2$. The result can be qualitatively explained by model calculations incorporating the lifting of the band inversion.

Single-crystalline $EuZn_2Sb_2$ (001) thin films were grown on CdTe (111)A substrates by the MBE technique following similar growth processes previously reported for other EuM_2X_2 films [24,25,31]. To remove oxides on the CdTe substrates, CdTe (111)A substrates were first etched by 0.01% Br_2-methanol, and then annealed around 550 °C under Cd flux before the $EuZn_2Sb_2$ growth. The growth temperature of the $EuZn_2Sb_2$ films was about 265 °C. The flux ratio of the three elements, Eu, Zn, and Sb, during the growth, was $P_{Eu} : P_{Zn} : P_{Sb} = 1 : 7–15 : 2–3$. We grew about 50-nm-thick films with a wide range of hole densities from 10^{19} to 10^{20} cm^{-3} by adjusting the flux ratio. Transport measurements were performed by making Hall bar devices from $EuZn_2Sb_2$ thin films and adopting a conventional four-probe method. Low-temperature

*Contact author: m.uchida@phys.sci.isct.ac.jp

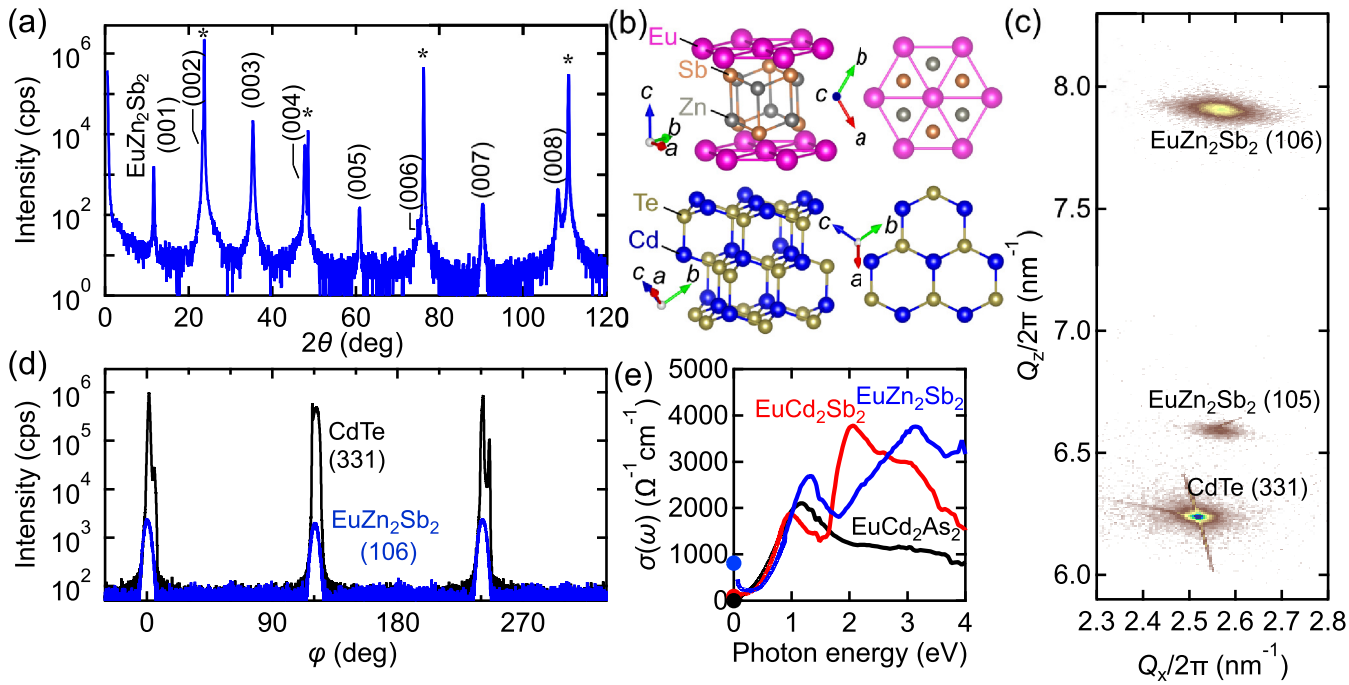

FIG. 1. Structural and optical characterization of $EuZn_2Sb_2$ thin films. (a) XRD θ-2θ scan of a $EuZn_2Sb_2$ thin film grown on a CdTe substrate. Substrate peaks are marked with an asterisk. (b) Epitaxial relation between $EuZn_2Sb_2$ and the CdTe substrate. (c) Reciprocal space map around CdTe (331), $EuZn_2Sb_2$ (105), and $EuZn_2Sb_2$ (106) peaks. (d) In-plane φ scans of CdTe (331) and $EuZn_2Sb_2$ (106) Bragg peaks. (e) Optical conductivity spectra of $EuZn_2Sb_2$, $EuCd_2Sb_2$, and $EuCd_2As_2$ films measured at room temperature. The dc conductivities are indicated by a solid circle.

magnetotransport was measured using a low-frequency lock-in technique in a Cryomagnetics cryostat system equipped with a superconducting magnet. Magnetization curves were measured using a superconducting quantum inference magnetometer in a Quantum Design magnetic property measurement system. We measured reflectivity spectra at room temperature using a Fourier transform spectrometer (the grating-type monochromator) in the photon energy region of 0.06–0.9 eV (0.7–4.6 eV), and then the optical conductivity spectra were obtained by a Kramers-Kronig analysis.

Figure 1(a) shows an x-ray diffraction (XRD) θ-2θ scan of a $EuZn_2Sb_2$ thin film. Clear peaks of the $EuZn_2Sb_2$ {001} series are observed along with the CdTe {111} series. To confirm the epitaxial relation as shown in Fig. 1(b), we performed reciprocal mapping including CdTe (331) and $EuZn_2Sb_2$ (105) and (106) Bragg peaks. The map in Fig. 1(c) indicates that the [100] $EuZn_2Sb_2$ film direction aligns with the $[11\bar{2}]$ direction of the CdTe substrate. The φ scan of CdTe (331) and $EuZn_2Sb_2$ (106) peaks in Fig. 1(d) ensures that the present $EuZn_2Sb_2$ film has only a single domain without 60° rotated domains. In Fig. 1(e), optical conductivity spectra obtained for the $EuZn_2Sb_2$ film are compared to films of two other EuA_2X_2 compounds, $EuCd_2Sb_2$ and $EuCd_2As_2$. The dc conductivity obtained from the transport measurement matches the extrapolation of the optical conductivity spectra to 0 eV. A peak at about 1 eV shifts toward higher energies in $EuZn_2Sb_2$, suggesting that the band inversion energy in $EuZn_2Sb_2$ is smaller than in $EuCd_2Sb_2$ and $EuCd_2As_2$, reflecting the weaker SOC.

To understand the fundamental magnetotransport of $EuZn_2Sb_2$ thin films, we first present their transport and magnetization measured under the out-of-plane field. Temperature dependences of the longitudinal resistivity ρ_{xx} in Fig. 2(a) and the magnetic susceptibility χ in Fig. 2(b) show a kink at 13.2 K, which is in good agreement with the Néel temperature T_N previously reported for $EuZn_2Sb_2$ bulk samples [27–30]. Especially above T_N, ρ_{xx} shows a metallic behavior. Application of an out-of-plane magnetic field below T_N leads to a simple magnetization curve where the antiferromagnetically ordered in-plane spin magnetic moments are gradually canted to the out-of-plane field direction. From both the magnetoresistivity curve in Fig. 2(c) and the magnetization curve in Fig. 2(d), the saturation field is estimated at 5.0 T. In the Hall resistivity ρ_{yx} shown in Fig. 2(c), the out-of-plane anomalous Hall effect is clearly observed even before subtracting the ordinary Hall component. A nonmonotonic anomalous Hall effect arising from the Berry curvature change during the magnetization process is also observed below the saturation field [26]. Figure 2(e) shows the anomalous Hall resistivity $\rho_{yx,AHE}$ for $EuZn_2Sb_2$ films with different carrier densities, obtained by subtracting the field-linear term from ρ_{yx}. $\rho_{yx,AHE}$ rapidly increases upon decreasing hole density. To confirm this trend more carefully, in Fig. 2(f) we plot the hole-density dependence of $\sigma_{xy,AHE,9T}/\sigma_{xx}^{1.6}$ calculated from the converted longitudinal conductivity σ_{xx} and the anomalous Hall conductivity at 9T $\sigma_{xy,AHE,9T}$, following the scaling relationship of the dirty metal region with impurity scattering [32]. In contrast to the case of the magnetic Weyl semimetal $EuCd_2Sb_2$, where $\sigma_{xy,AHE,9T}/\sigma_{xx}^{1.6}$ is maximized with the Fermi energy tuned to the Weyl points energy range [24,25], $\sigma_{xy,AHE,9T}/\sigma_{xx}^{1.6}$ continues to increase with a decrease

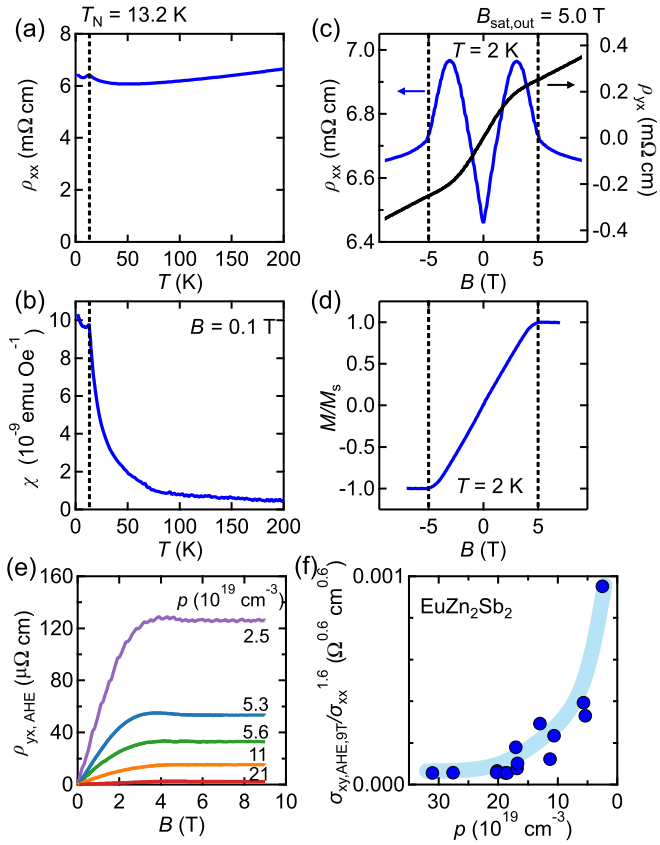

FIG. 2. Fundamental magnetotransport of $EuZn_2Sb_2$ thin films. Temperature dependences of (a) longitudinal resistivity ρ_{xx} and (b) magnetic susceptibility χ. The Néel temperature T_N of 13.2 K is indicated by a dashed line. (c) Magnetic field dependence of ρ_{xx} and Hall resistivity ρ_{yx}, and (d) a magnetization curve, taken under the out-of-plane magnetic field at 2 K. The hole density of the sample for (a)–(d) is 5.6×10^{19} cm^{-3}. The out-of-plane saturation field $B_{sat,out}$ is determined to be 5.0 T. (e) Anomalous Hall resistivity $\rho_{yx,AHE}$ extracted for $EuZn_2Sb_2$ films with different hole densities is at 2 K. (f) Hole-density dependence of $\sigma_{xy,AHE,9T}/\sigma_{xx}^{1.6}$, clearly revealing the large enhancement with decrease in the hole density.

in the hole density in $EuZn_2Sb_2$. This suggests the presence of Berry curvature hot spots in the higher Fermi energy range in $EuZn_2Sb_2$.

Next, we move on to magnetotransport under the in-plane magnetic field. The electric current is applied along the [110] direction of $EuZn_2Sb_2$ and the in-plane magnetic field is rotated with the azimuthal angle φ measured from the [110] direction as shown in Fig. 3. We analyzed the raw φ-scan data to separate different in-plane phenomena as the twofold planar Hall effect (PHE) and the threefold in-plane anomalous Hall effect [33]. A comprehensive data analysis of PHE is provided in the Supplemental Material [34] (see also Refs. [35,36] therein). As detailed therein, we observed a sign reversal in the PHE resistivity ($\rho_{yx,PHE}$) and the anisotropic magnetoresistivity (AMR) ($\rho_{xx,AMR}$) [37–41].

The observed IAHE can be explained by the orbital magnetization model as in $EuCd_2Sb_2$ [4], where the out-of-plane Berry curvature and orbital magnetization components are induced by the in-plane magnetic field. The octupole model considering the higher order of spin magnetization is not applicable in the present case, since out-of-plane tilting of the Hall vector by this effect occurs only when the measurement plane is not a principal plane [5]. In addition, according to the anomalous orbital polarizability model [18], tensor components responsible for IAHE are zero in D_{3d} systems. Figure 3(c) presents the in-plane field dependence of $\rho_{yx,AHE}$ at $\varphi = 30^\circ$. This field dependence seen in $\rho_{yx,AHE}$ is completely different from the $\rho_{yx,PHE}$ one. It is also noticeable that $\rho_{yx,AHE}$ keeps increasing even above $B_{sat,in}$. This is because the Zeeman-type band splitting continues to increase and the resulting orbital magnetization keeps changing even above the saturation field of the spin magnetization [4,42,43].

Figure 3 shows a comparison of the IAHE between the $EuZn_2Sb_2$ and $EuCd_2Sb_2$ films. The azimuthal angle φ is measured from the [110] direction as illustrated in the inset of Fig. 3, where the Zn/Cd atoms are located in the same positions in $EuZn_2Sb_2/EuCd_2Sb_2$. Primarily there are two important differences: First, the sign of IAHE especially above $B_{sat,in}$ is opposite in the two compounds. As confirmed in Figs. 3(a) and 3(b), the 9-T curve is negative, for example, at $\varphi = 30^\circ$ in $EuCd_2Sb_2$ but positive in $EuZn_2Sb_2$. This can be confirmed also in the magnetic field scans in Figs. 3(c) and 3(d), suggesting the possibility that the out-of-plane orbital magnetization points in opposite directions between the two compounds. Second, the field dependence of the IAHE below $B_{sat,in}$ is different. In the $EuCd_2Sb_2$ film, $\rho_{yx,AHE}$ exhibits a nonmonotonic behavior characterized by a pronounced peak at 0.7 T. This peak can be explained by the nonmonotonic change of the Berry curvature during the formation and shifting of the Weyl points near the Fermi energy during the magnetization process [26,44]. On the other hand, such nonmonotonic dependence is hardly seen in $EuZn_2Sb_2$.

To identify the origin of the differences in IAHE, we have performed the calculation of anomalous Hall conductivity using a microscopic model. According to previous studies [45], the bands of $EuCd_2Sb_2$ near the Fermi level at Γ point consist of Cd 5*s* bands and Sb 5*p* bands, where the conduction band mainly consists of Cd $^2S_{1/2}$ and Sb $^2P_{1/2}$ orbitals, and the Sb $^2P_{3/2}$ orbitals construct the valence band. As the Fermi level of our $EuZn_2Sb_2$ thin films lies in the valence band, here we consider the four valence bands arising from the Sb $^2P_{3/2}$ orbitals for our model [46]. The effective model near the Γ point is

$$H_0 = d_0(\vec{k}) + \sum_{i=1}^{5} d_i(\vec{k})\Gamma_i, \tag{1}$$

where $d_0(\vec{k}) = \mu + a_z^0 k_z^2 + a_\perp^0 (k_z^2 + k_y^2)$, $d_1(\vec{k}) = \sqrt{3}[E_{11} k_y k_z + E_{21}(k_y^2 - k_x^2)]$, $d_2(\vec{k}) = \sqrt{3}[E_{11} k_x k_z - 2E_{21} K_x k_y]$, $d_3(\vec{k}) = \sqrt{3}[-E_{12} k_x k_z + 2E_{22} k_x k_y]$, $d_4(\vec{k}) = \sqrt{3}[E_{22}(k_x^2 - k_y^2) - E_{12} k_y k_z]$, and $d_5(\vec{k}) = \Delta + a_z^z k_z^2 + a_\perp^z (k_z^2 + k_y^2)$ [4]. The matrices $\Gamma_1 = \sigma^3 \otimes \sigma^2$, $\Gamma_2 = \sigma^3 \otimes \sigma^1$, $\Gamma_3 = \sigma^2 \otimes \sigma^0$, $\Gamma_4 = \sigma^1 \otimes \sigma^0$, and $\Gamma_5 = \sigma^3 \otimes \sigma^3$ are time-reversal symmetric 4×4 matrices [46], where $\sigma^{1,2,3}$ are the Pauli matrices, and σ^0 is the 2×2 unit matrix.

The bands hosting the Weyl point pairs near the Γ point are dominated by the Sb $^2P_{3/2}$ orbitals in $EuCd_2Sb_2$ [45].

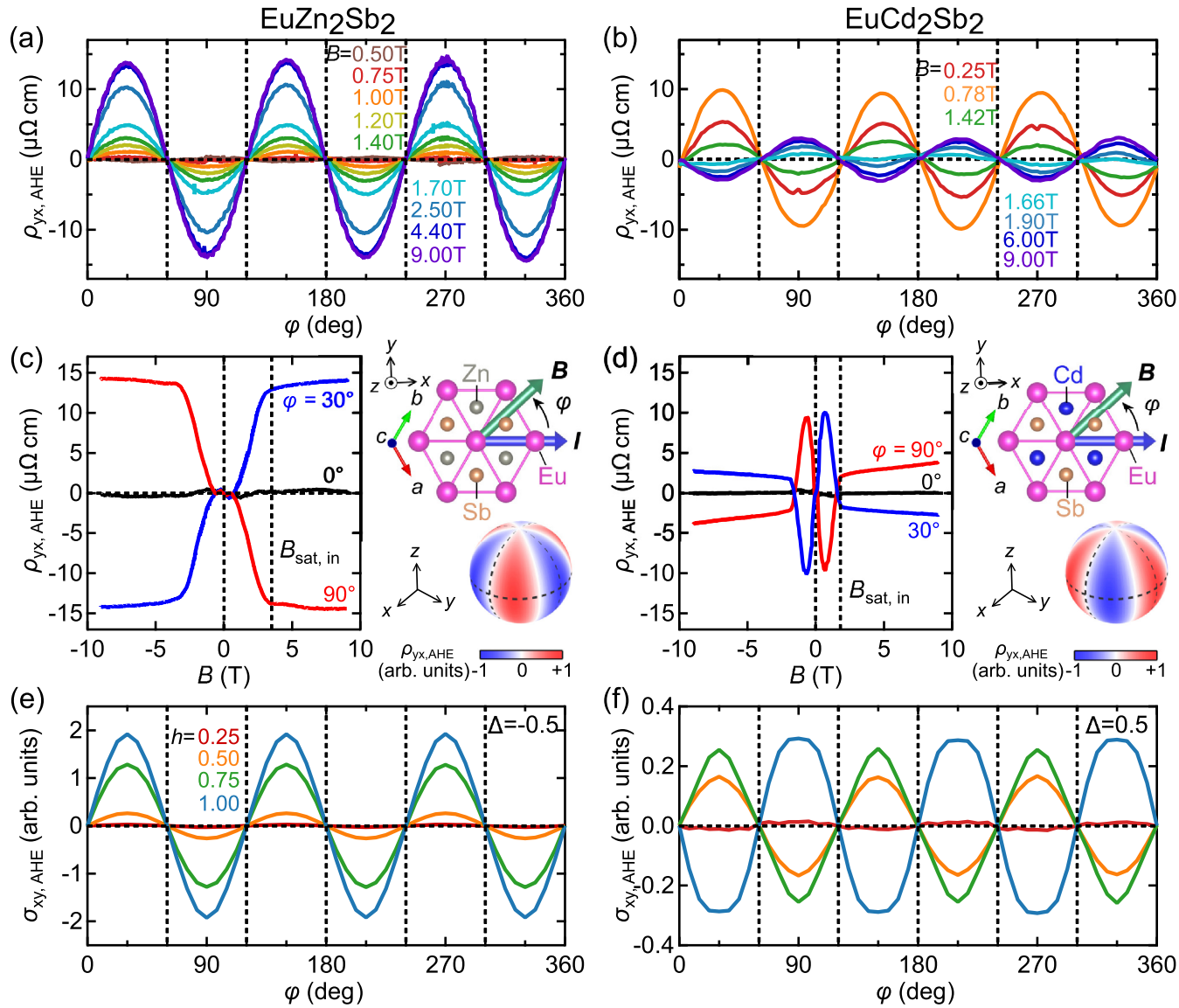

FIG. 3. Comparison of the in-plane anomalous Hall resistivity between $EuZn_2Sb_2$ and $EuCd_2Sb_2$. In-plane field angle dependence of $\rho_{yx,AHE}$ taken for (a) $EuZn_2Sb_2$ and (b) $EuCd_2Sb_2$ films at various magnetic fields. In-plane field scans of $\rho_{yx,AHE}$ for the (c) $EuZn_2Sb_2$ and (d) $EuCd_2Sb_2$ films at specific angles of $\varphi = 0°$, 30°, and 90°. The schematic on the right illustrates the measurement configuration with respect to the crystal axes and field angle dependence of $\rho_{yx,AHE}$ observed above $B_{sat,in}$. In-plane field angle dependence of the anomalous Hall conductivity $\sigma_{xy,AHE}$, calculated for the band splitting parameters (e) $\Delta = -0.5$ and (f) $\Delta = 0.5$ at different fields $h = B/B_{sat,in}$ below $B_{sat,in}$.

The effect of the chemical substitution between Cd and Zn results in the change of lattice parameter, especially the uniaxial anisotropy c/a. The band inversion is modulated by the change of uniaxial anisotropy, which is effectively expressed by the parameter Δ. To understand the effect of Δ, we compare the anomalous Hall conductivity $\sigma_{xy,AHE}$ by simply changing the band splitting parameter Δ; the other parameters are fixed to $\mu = -1.5$, $a_z^0 = a_\perp^0 = -2.0$, $a_z^z = -0.5$, $a_\perp^z = 0.25$, $E_{11} = -E_{21} = -0.5$, and $E_{12} = E_{22} = 0$. The calculated ϕ dependence for $\Delta = -0.5$ and 0.5 is shown in Figs. 3(e) and 3(f), respectively, with the latter corresponding to an inverted band structure with Weyl points. $\sigma_{xy,AHE}$ calculated for $\Delta = -0.5$ is positive at $\varphi = 30°$ and monotonically increases with an increase in the in-plane magnetic field. On the other hand, $\sigma_{xy,AHE}$ calculated for $\Delta = 0.5$ nonmonotonically changes with sign inversion and exhibits a negative value at the saturation field ($h = B/B_{sat,in} = 1$). These features found for $\Delta = -0.5$ and 0.5 are quite similar to the observations in $EuZn_2Sb_2$ and $EuCd_2Sb_2$, respectively.

To see the effect of Δ more clearly, we present the Δ dependence of anomalous Hall conductivity $\sigma_{xy,AHE}$. The band dispersion with $\Delta = -0.5$ and $\Delta = 0.5$ are also shown in Figs. 4(b) and 4(c), respectively. There is a band crossing between the Sb $5p$ bands in the case of $\Delta = 0.5$, while there is not for $\Delta = -0.5$. The anomalous Hall conductivity changes its sign around the region where the band inversion is lifted.

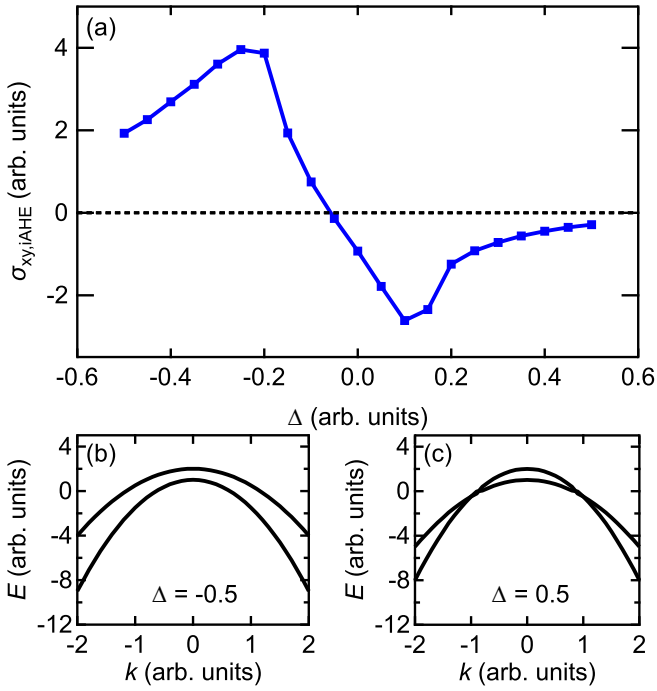

FIG. 4. Relation between in-plane anomalous Hall conductivity and the parameter Δ representing the band modulation through the uniaxial anisotropy. (a) Δ dependence of in-plane anomalous Hall conductivity at $\varphi = 30°$. Band dispersions with (b) $\Delta = -0.5$ and (c) $\Delta = 0.5$.

By changing the band inversion parameter Δ related to uniaxial anisotropy, the drastic change in the IAHE response as confirmed between $EuZn_2Sb_2$ and $EuCd_2Sb_2$ can be simply demonstrated.

In summary, we have studied the in-plane anomalous Hall effect in single-crystalline films of $EuZn_2Sb_2$, which is a good reference material with a weaker SOC than in $EuCd_2Sb_2$. The in-plane anomalous Hall effect clearly appears with a threefold azimuthal angle dependence in addition to the conventional twofold planar Hall effect. In comparison to $EuCd_2Sb_2$, $EuZn_2Sb_2$ exhibits the in-plane anomalous Hall resistivity with opposite sign and a rather a monotonic field dependence. These differences are qualitatively reproduced in our model calculations by simply changing the band inversion parameter caused by uniaxial anisotropy. Our findings lay the groundwork for systematically controlling the in-plane anomalous Hall effect and orbital magnetization through elaborate band engineering.

This work was supported by JST FOREST Program Grant No. JPMJFR202N, Japan, by Grant-in-Aids for Scientific Research No. JP22K18967, No. JP22K20353, No. JP23K13666, No. JP23K03275, No. JP24H01614, and No. JP24H01654 from MEXT, Japan, by Murata Science and Education Foundation, Japan, by Iketani Science and Technology Foundation, Japan, and by STAR Award funded by the Tokyo Tech Fund, Japan.

[1] N. Nagaosa, J. Sinova, S. Onoda, A. H. MacDonald, and N. P. Ong, Anomalous Hall effect, Rev. Mod. Phys. **82**, 1539 (2010).

[2] Z. Fang, N. Nagaosa, K. S. Takahashi, A. Asamitsu, R. Mathieu, T. Ogasawara, H. Yamada, M. Kawasaki, Y. Tokura, and K. Terakura, The anomalous Hall effect and magnetic monopoles in momentum space, Science **302**, 92 (2003).

[3] Y. Yao, L. Kleinman, A. H. MacDonald, J. Sinova, T. Jungwirth, D.-S. Wang, E. Wang, and Q. Niu, First principles calculation of anomalous Hall conductivity in ferromagnetic bcc Fe, Phys. Rev. Lett. **92**, 037204 (2004).

[4] A. Nakamura, S. Nishihaya, H. Ishizuka, M. Kriener, Y. Watanabe, and M. Uchida, In-plane anomalous Hall effect associated with orbital magnetization: Measurements of low-carrier density films of a magnetic Weyl semimetal, Phys. Rev. Lett. **133**, 236602 (2024).

[5] W. Peng, Z. Liu, H. Pan, P. Wang, Y. Chen, J. Zhang, X. Yu, J. Shen, M. Yang, Q. Niu *et al.*, Observation of the in-plane anomalous Hall effect induced by octupole in magnetization space, arXiv:2402.15741.

[6] X. Liu, H.-C. Hsu, and C.-X. Liu, In-plane magnetization-induced quantum anomalous Hall effect, Phys. Rev. Lett. **111**, 086802 (2013).

[7] Y. Ren, J. Zeng, X. Deng, F. Yang, H. Pan, and Z. Qiao, Quantum anomalous Hall effect in atomic crystal layers from in-plane magnetization, Phys. Rev. B **94**, 085411 (2016).

[8] J. Zhang, Z. Liu, and J. Wang, In-plane magnetic-field-induced quantum anomalous Hall plateau transition, Phys. Rev. B **100**, 165117 (2019).

[9] Y. Ren, Z. Qiao, and Q. Niu, Engineering corner states from two-dimensional topological insulators, Phys. Rev. Lett. **124**, 166804 (2020).

[10] S. Sun, H. Weng, and X. Dai, Possible quantization and half-quantization in the anomalous Hall effect caused by in-plane magnetic field, Phys. Rev. B **106**, L241105 (2022).

[11] Z. Li, Y. Han, and Z. Qiao, Chern number tunable quantum anomalous Hall effect in monolayer transitional metal oxides via manipulating magnetization orientation, Phys. Rev. Lett. **129**, 036801 (2022).

[12] L. Li, J. Cao, C. Cui, Z.-M. Yu, and Y. Yao, Planar Hall effect in topological Weyl and nodal-line semimetals, Phys. Rev. B **108**, 085120 (2023).

[13] J. Cao, W. Jiang, X.-P. Li, D. Tu, J. Zhou, J. Zhou, and Y. Yao, In-plane anomalous Hall effect in $\mathcal{PT}$-symmetric antiferromagnetic materials, Phys. Rev. Lett. **130**, 166702 (2023).

[14] T. Liang, J. Lin, Q. Gibson, S. Kushwaha, M. Liu, W. Wang, H. Xiong, J. A. Sobota, M. Hashimoto, P. S. Kirchmann *et al.*, Anomalous Hall effect in $ZrTe_5$, Nat. Phys. **14**, 451 (2018).

[15] J. Zhou, W. Zhang, Y.-C. Lin, J. Cao, Y. Zhou, W. Jiang, H. Du, B. Tang, J. Shi, B. Jiang *et al.*, Heterodimensional superlattice with in-plane anomalous Hall effect, Nature (London) **609**, 46 (2022).

[16] L. Wang, J. Zhu, H. Chen, H. Wang, J. Liu, Y.-X. Huang, B. Jiang, J. Zhao, H. Shi, G. Tian *et al.*, Orbital magneto-nonlinear anomalous Hall effect in kagome magnet Fe_3Sn_2, Phys. Rev. Lett. **132**, 106601 (2024).

[17] V. A. Zyuzin, In-plane Hall effect in two-dimensional helical electron systems, Phys. Rev. B **102**, 241105(R) (2020).
[18] H. Wang, Y.-X. Huang, H. Liu, X. Feng, J. Zhu, W. Wu, C. Xiao, and S. A. Yang, Orbital origin of the intrinsic planar Hall effect, Phys. Rev. Lett. **132**, 056301 (2024).
[19] R. Battilomo, N. Scopigno, and C. Ortix, Anomalous planar Hall effect in two-dimensional trigonal crystals, Phys. Rev. Res. **3**, L012006 (2021).
[20] J. H. Cullen, P. Bhalla, E. Marcellina, A. R. Hamilton, and D. Culcer, Generating a topological anomalous Hall effect in a nonmagnetic conductor: An in-plane magnetic field as a direct probe of the Berry curvature, Phys. Rev. Lett. **126**, 256601 (2021).
[21] E. Roman, Y. Mokrousov, and I. Souza, Orientation dependence of the intrinsic anomalous Hall effect in hcp cobalt, Phys. Rev. Lett. **103**, 097203 (2009).
[22] D. Li, M. Wang, D. Li, and J. Zhou, Switchable in-plane anomalous Hall effect by magnetization orientation in monolayer $Mn_3Si_2Te_6$, Phys. Rev. B **109**, 155153 (2024).
[23] L.-L. Wang, N. H. Jo, B. Kuthanazhi, Y. Wu, R. J. McQueeney, A. Kaminski, and P. C. Canfield, Single pair of Weyl fermions in the half-metallic semimetal $EuCd_2As_2$, Phys. Rev. B **99**, 245147 (2019).
[24] H. Su, B. Gong, W. Shi, H. Yang, H. Wang, W. Xia, Z. Yu, P.-J. Guo, J. Wang, L. Ding *et al.*, Magnetic exchange induced Weyl state in a semimetal $EuCd_2Sb_2$, APL Mater. **8**, 011109 (2020).
[25] M. Ohno, S. Minami, Y. Nakazawa, S. Sato, M. Kriener, R. Arita, M. Kawasaki, and M. Uchida, Maximizing intrinsic anomalous Hall effect by controlling the Fermi level in simple Weyl semimetal films, Phys. Rev. B **105**, L201101 (2022).
[26] A. Nakamura, S. Nishihaya, H. Ishizuka, M. Kriener, M. Ohno, Y. Watanabe, M. Kawasaki, and M. Uchida, Berry curvature derived negative magnetoconductivity observed in type-II magnetic Weyl semimetal films, Phys. Rev. B **109**, L121108 (2024).
[27] M. X. Sprague, S. Regmi, B. Ghosh, A. P. Sakhya, M. I. Mondal, I. Bin Elius, N. Valadez, B. Singh, T. Romanova, D. Kaczorowski *et al.*, Observation of paramagnetic spin-degeneracy lifting in $EuZn_2Sb_2$, Phys. Rev. B **110**, 045130 (2024).
[28] F. Weber, A. Cosceev, S. Drobnik, A. Faisst, K. Grube, A. Nateprov, C. Pfleiderer, M. Uhlarz, and H. v. Löhneysen, Low-temperature properties and magnetic order of $EuZn_2Sb_2$, Phys. Rev. B **73**, 014427 (2006).
[29] H. Zhang, J.-T. Zhao, Y. Grin, X.-J. Wang, M.-B. Tang, Z.-Y. Man, H.-H. Chen, and X.-X. Yang, A new type of thermoelectric material, $EuZn_2Sb_2$, J. Chem. Phys. **129**, 164713 (2008).
[30] K. Singh, O. Pavlosiuk, S. Dan, D. Kaczorowski, and P. Wiśniewski, Large unconventional anomalous Hall effect arising from spin chirality within domain walls of an antiferromagnet $EuZn_2Sb_2$, Phys. Rev. B **109**, 125107 (2024).
[31] S. Nishihaya, A. Nakamura, M. Ohno, M. Kriener, Y. Watanabe, M. Kawasaki, and M. Uchida, Intrinsic insulating transport characteristics in low-carrier density $EuCd_2As_2$ films, Appl. Phys. Lett. **124**, 023103 (2024).
[32] S. Onoda, N. Sugimoto, and N. Nagaosa, Quantum transport theory of anomalous electric, thermoelectric, and thermal Hall effects in ferromagnets, Phys. Rev. B **77**, 165103 (2008).
[33] T. Kurumaji, Symmetry-based requirement for the measurement of electrical and thermal Hall conductivity under an in-plane magnetic field, Phys. Rev. Res. **5**, 023138 (2023).
[34] See Supplemental Material at http://link.aps.org/supplemental/10.1103/PhysRevB.111.L241106 for analysis details, which includes Refs. [35–38,40].
[35] S. Kokado, M. Tsunoda, K. Harigaya, and A. Sakuma, Anisotropic magnetoresistance effects in Fe, Co, Ni, Fe_4N, and half-metallic ferromagnet: A systematic analysis, J. Phys. Soc. Jpn. **81**, 024705 (2012).
[36] M. Uchida, W. Sano, K. Takahashi, T. Koretsune, Y. Kozuka, R. Arita, Y. Tokura, and M. Kawasaki, Field-direction control of the type of charge carriers in nonsymmorphic IrO_2, Phys. Rev. B **91**, 241119 (2015).
[37] W. Thomson, On the electro-dynamic qualities of metals:—Effects of magnetization on the electric conductivity of nickel and of iron, Proc. R. Soc. Lond. **8**, 546 (1857).
[38] T. McGuire and R. Potter, Anisotropic magnetoresistance in ferromagnetic 3d alloys, IEEE Trans. Magn. **11**, 1018 (1975).
[39] A. A. Burkov, Giant planar Hall effect in topological metals, Phys. Rev. B **96**, 041110(R) (2017).
[40] S. Nandy, G. Sharma, A. Taraphder, and S. Tewari, Chiral anomaly as the origin of the planar Hall effect in Weyl semimetals, Phys. Rev. Lett. **119**, 176804 (2017).
[41] N. Kumar, S. N. Guin, C. Felser, and C. Shekhar, Planar Hall effect in the Weyl semimetal GdPtBi, Phys. Rev. B **98**, 041103(R) (2018).
[42] A. A. Burkov and L. Balents, Weyl semimetal in a topological insulator multilayer, Phys. Rev. Lett. **107**, 127205 (2011).
[43] N. Ito and K. Nomura, Anomalous Hall effect and spontaneous orbital magnetization in antiferromagnetic Weyl metal, J. Phys. Soc. Jpn. **86**, 063703 (2017).
[44] K. S. Takahashi, H. Ishizuka, T. Murata, Q. Y. Wang, Y. Tokura, N. Nagaosa, and M. Kawasaki, Anomalous Hall effect derived from multiple Weyl nodes in high-mobility $EuTiO_3$ films, Sci. Adv. **4**, eaar7880 (2018).
[45] J.-R. Soh, C. Donnerer, K. M. Hughes, E. Schierle, E. Weschke, D. Prabhakaran, and A. T. Boothroyd, Magnetic and electronic structure of the layered rare-earth pnictide $EuCd_2Sb_2$, Phys. Rev. B **98**, 064419 (2018).
[46] S. Murakami, N. Nagaosa, and S.-C. Zhang, SU(2) non-Abelian holonomy and dissipationless spin current in semiconductors, Phys. Rev. B **69**, 235206 (2004).